JACS
JOURNAL OF THE AMERICAN CHEMICAL SOCIETY
pubs.acs.org/JACS
Article

Unraveling Serial Degradation Pathways of Supported Catalysts through Reliable Electrochemical Liquid-Cell TEM Analysis

Sungin Kim, Jimin Kwag, Minyoung Lee, Sungsu Kang, Dongjun Kim, Jong-Gil Oh, Young-Jung Heo,* Jaeyune Ryu,* and Jungwon Park*

Cite This: https://doi.org/10.1021/jacs.4c08825
Read Online

ABSTRACT: Electrochemical liquid-cell transmission electron microscopy (e-LCTEM) offers great potential for investigating the structural dynamics of nanomaterials during electrochemical reactions. However, challenges arise from the difficulty in achieving the optimal electrolyte thickness, leading to inconsistent electrochemical responses and limited spatial resolution. In this study, we present advanced e-LCTEM techniques tailored for tracking Pt/C degradation under electrochemical polarization at short intervals with high spatial resolution. Our innovative approach combines microfabrication-based sample preparation with *in situ* control of electrolyte thickness, ensuring reliable electrochemical signal acquisition and direct observation of sequential catalyst degradation. Quantitative imaging analyses conducted at both global areas and single-particle levels unveil a distinctive degradation mechanism primarily driven by nanoparticle migrations. Smaller nanoparticles exhibit a higher susceptibility to migration, leading to coalescence and final detachment in series. This migration-gated degradation mechanism provides a new perspective on the size-dependent durability of supported nanoparticles, complementing the prevailing explanation centered on the size-dependent dissolution kinetics of nanoparticles.

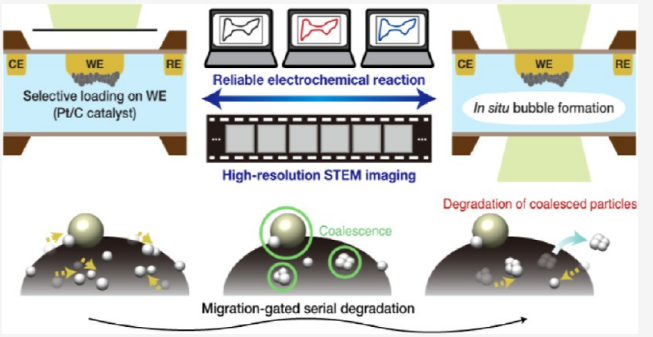

INTRODUCTION

Supported catalysts are central to energy conversion and storage devices, including fuel cells, electrolyzers, and batteries.[1−11] Typically, these catalysts consist of metal nanoparticles supported on conductive materials such as carbon or metal oxides.[2−4,12] Carbon-based supports are particularly favored due to their high surface area and excellent electrical conductivity, facilitating the dispersion of metal nanoparticles and promoting electron transfer during electrochemical reactions.[1−5,12−14] Despite the widespread use of carbon-supported catalysts, however, challenges persist in optimizing their stability against degradation under electrochemical conditions,[1−3,12,15,16] necessitating a deep understanding of degradation mechanisms.

Structural dynamics of nanoparticles under electrochemical polarization is not only determined by particle dissolution trends but also gated by the interaction between catalyst particles and supports.[13,17,18] Electrochemical polarization is known to mitigate the electronic and electrostatic interactions between nanoparticles and carbon supports; however, the detailed mechanism of the structural evolutions of nanoparticles driven by these perturbations remains largely elusive.[1−3,12,13,17−19] Previous post-mortem and identical-location transmission electron microscopy (TEM)-based analysis has identified various degradation phenomena such as support corrosion, dissolution, coalescence, migration, and particle detachment. However, these *ex situ* studies, without a proper time frame of image acquisition, provide in most cases only an overlap of multiple pathways, which lacks insights into a full mechanistic picture that can explain the dynamic nature of the catalyst evolution under polarization.

The electrochemical liquid-cell TEM (e-LCTEM) technique has the potential to directly observe the structural dynamics of catalysts at solid−liquid interfaces under electrical bias in real time.[20−27] While some e-LCTEM studies have explored the degradation of Pt-based nanoparticles on carbon supports (Pt/C), these studies fall short in providing a full comprehensive mechanism.[28−33] Critically, the electrochemical responses measured under previous e-LCTEM conditions often deviate significantly from those recorded under normal electrochemical conditions, raising concerns regarding the reliability and integrity of the e-LCTEM studies. To avoid abnormal electrochemical responses from the e-LCTEM setup, a thick

Received: June 30, 2024
Revised: December 6, 2024
Accepted: December 9, 2024

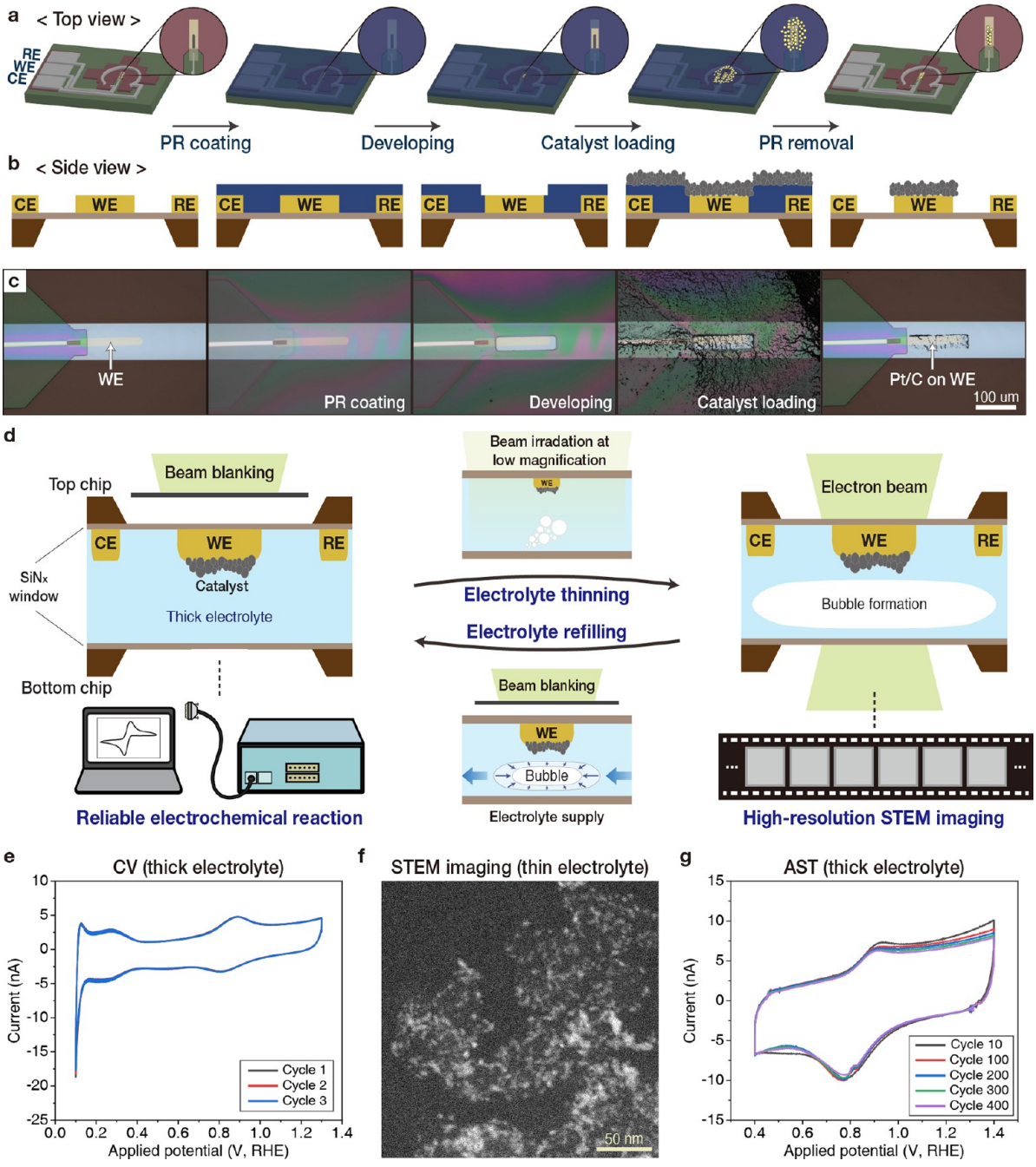

Figure 1. Selective catalyst loading and electrolyte thinning–refilling strategy. (a,b) Illustration of the selective loading of the catalyst on the top chip. The microfabrication processes are presented from the top (a) and side view (b). (c) Optical microscope images of each fabrication process; scale bar, 100 μm. (d) A scheme of the electrolyte thinning–refilling strategy. (e) CV curves of the Pt/C catalyst measured in the thick electrolyte condition with 3 cycles. (f) The STEM image of Pt/C obtained in the thin electrolyte condition; scale bar, 50 nm. (g) CV profiles of Pt/C under AST up to 400 cycles measured in the thick electrolyte condition.

electrolyte of several micrometers is typically introduced into the liquid-cell, providing a conductive environment suitable for three-electrode experiments.[34] However, imaging through such a thick electrolyte results in substantial electron-beam (e-beam) scattering, compromising the spatial resolution for imaging small catalyst domains (<10 nm).[24]

To mitigate this parasitic trade-off, we present herein a novel e-LCTEM technique integrated with advanced sample preparation and *in situ* thickness control of the electrolyte (Figure 1a–d). This innovation enables a time-series analysis of high-resolution scanning transmission electron microscopy (STEM) images for small Pt nanoparticles (<3 nm) while ensuring reliable electrochemical reactions within confined electrolytes (Figure 1e–g). Using this tool, we explore the degradation processes of representative ORR catalysts, comprising Pt nanoparticles with varying sizes and loading amounts on carbon supports, under accelerated stress test (AST) conditions that simulate start–stop operations of the fuel cell.[19,35,36] Our analytic protocol applied for this system allows for decoupling of overlapped degradation pathways and the direct observation of sequential processes. Through quantitative and direct imaging analysis at both global areas

https://doi.org/10.1021/jacs.4c08825
J. Am. Chem. Soc. XXXX, XXX, XXX–XXX

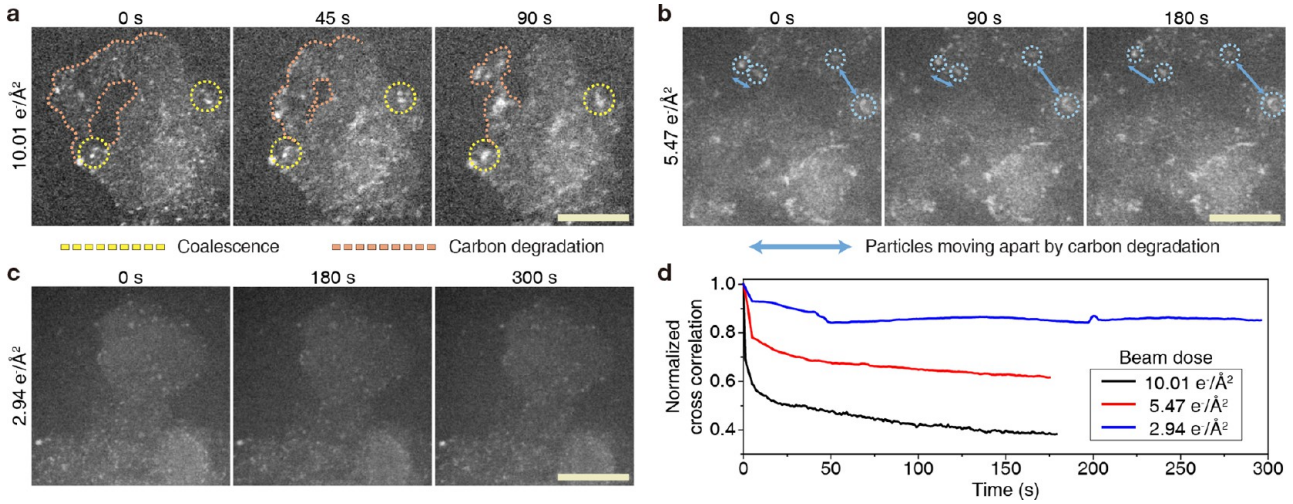

Figure 2. Fine control of an e-beam dose. (a–c) Snapshots of STEM movies for the Pt/C catalysts under e-beam irradiation with different e-beam doses; scale bars, 100 nm. The e-beam doses are 10.01 (a), 5.47 (b), and 2.94 $e^-/Å^2$ (c), respectively. (d) Normalized cross-correlations of the three STEM movies. The black, red, and blue profiles represent the normalized cross-correlations of the STEM movies under e-beam doses of 10.01, 5.47, and 2.94 $e^-/Å^2$, respectively.

and single-particle levels, we uncover a distinct catalyst degradation mechanism predominantly gated by migration of Pt nanoparticles.

RESULTS AND DISCUSSION

Advancing e-LCTEM Protocols. We developed advanced e-LCTEM protocols to acquire desirable spatial resolutions and reliable electrochemical responses. The liquid-cell consists of a top chip containing three micropatterned electrode compartments and a bottom chip, both equipped with e-beam transparent silicon nitride windows (Figure S1). The micrometer-scale dimensions of the glassy carbon working electrode compartment make selective drop-casting or slurry deposition of catalysts difficult, leading to undesirable catalyst loading across other electrode compartments to cause short circuits or unexpected electrothermal responses (Figure S2a). To solve this issue, we implemented a photolithographic treatment (Figure 1a–c and Materials and Methods, Supporting Information). After spin-coating of the negative photoresist (PR) on the top chip, UV exposure is applied on the PR-coated chip with a photomask that blocks the region of the working electrode compartment (Figure S3). The UV-exposed chip is then immersed in a developer solution to selectively remove the PR from the region of the working electrode. A well-dispersed solution of Pt/C catalysts is drop-cast onto the PR-patterned chip. Finally, removal of the remaining PR results in the selective loading of Pt/C catalysts onto the working electrode (Figures 1a–c and S2b). The developer solution has a minimal impact on the active sites of the Pt/C catalysts, as evidenced by the electrochemical active surface area (ECSA) calculation of the Pt/C catalyst after immersion in the developer solution using a rotating disk electrode (RDE) (Figure S4). The assembled liquid-cell with the catalyst-loaded chip is then filled by flowing a 0.1 M $HClO_4$ electrolyte (Figure 1d). The selective loading of a sufficient amount of Pt/C catalyst onto the working electrode enhanced electrochemical signals without unwanted electrochemical responses (Figures 1e and S2c), as evidenced by the recorded CV spectra featuring characteristic H adsorption/desorption and Pt oxide formation/reduction peaks.[35,37,38] Additionally, the positions of the OCP values on the CV profiles of Pt/C catalysts obtained in the e-LCTEM and a RDE are comparable, indicating the reliability of the electrochemical environment in e-LCTEM (Figure S5).

We next established an experimental strategy to control electrolyte thickness, enabling the observation of the degradation process of Pt/C catalysts with high resolution in reliable electrochemical reactions. In the thick electrolyte, sufficient connection in the three-electrode system patterned on the top chip under beam blanking conditions facilitated reliable electrochemical polarization (Figure 1d, left). Coupled with the increased hydrophilicity of the top chip through an O_2 plasma treatment (Materials and Methods, Supporting Information), low-dose irradiation of the e-beam at low magnification (50×) induced a slow generation of a bubble within the liquid-cell (Figure 1d, middle, and Movie S1). This control enhanced spatial resolution with reduced thickness of the electrolyte (Figure 1d, right), allowing for the acquisition of high-resolution STEM images (Figure 1d,f). The bubble can be eliminated by introducing an additional fresh electrolyte into the liquid-cell (Figure 1d, middle), restoring the electrolyte thickness to a sufficient level for conducting reliable electrochemical reactions (Figure 1d,g). This thinning and refilling process can be repeated while potential-induced structural changes are monitored in the catalysts (Figure 1d). Notably, the gradual formation of the bubble does not affect the locations of catalysts, allowing for the observation of the same region of catalysts over successive electrochemical reactions.

The e-beam, used as an imaging probe, potentially interacts with materials of observation, causing physicochemical damage to the observing material. Thus, careful use of the e-beam is required to ensure high reliability of the e-LCTEM experiments.[20,33,39,40] Given that the beam effect is more pronounced as the liquid layer is thinner, we conducted STEM imaging with varying e-beam doses on commercial $Pt_{10\ wt\ \%}/C$ catalysts in a thin liquid layer less than 500 nm without electrical biasing (Figure 2a–d and Movie S2). When exposed to a continuous e-beam dose of 10.01 $e^-/Å^2$ over 150 s, the Pt/C catalyst exhibited coalescence of the Pt nanoparticles and aggressive

https://doi.org/10.1021/jacs.4c08825
J. Am. Chem. Soc. XXXX, XXX, XXX−XXX

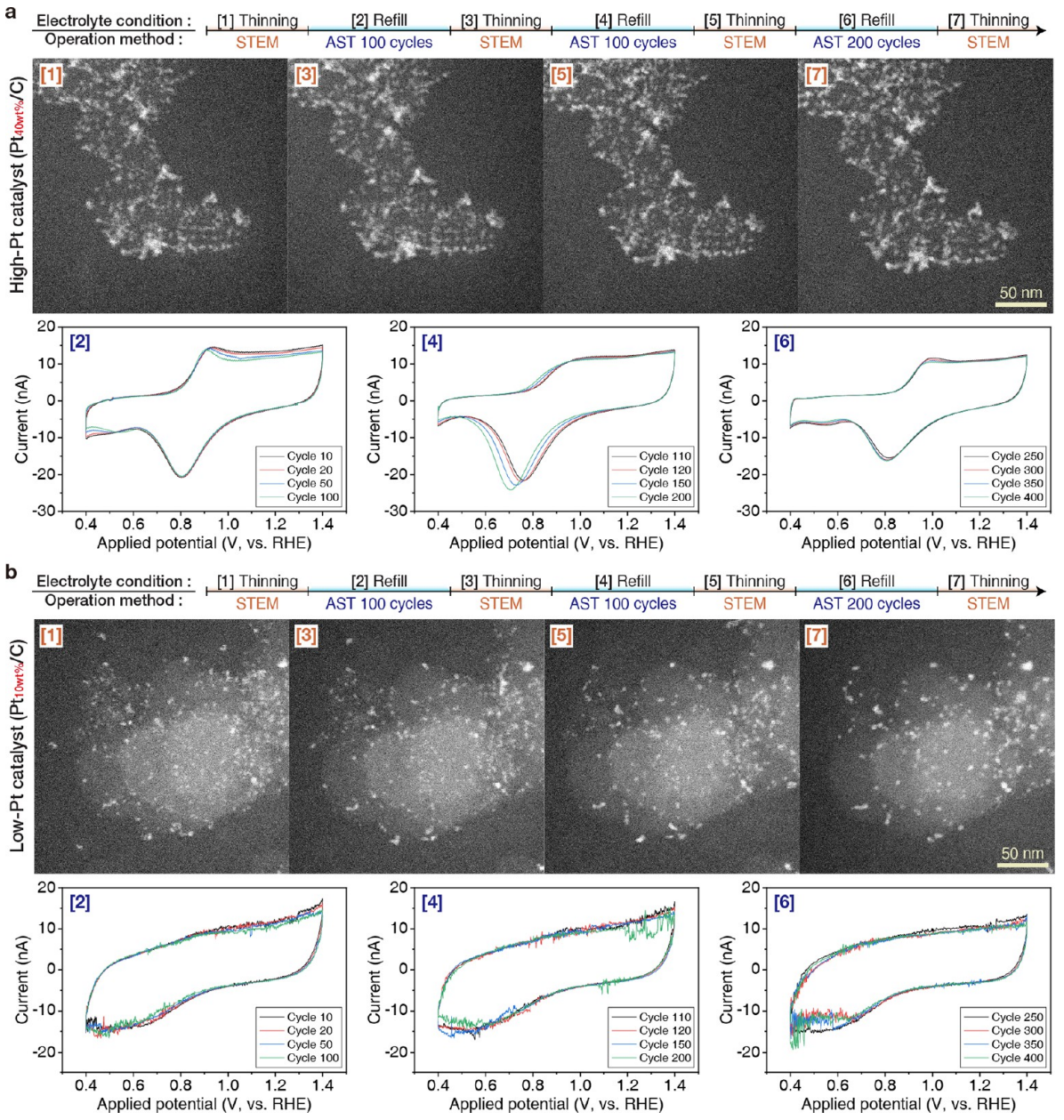

Figure 3. The results of e-LCTEM experiments with reliable electrochemical reactions for the commercial Pt/C catalysts. (a,b) Alternately obtained STEM images and CV profiles by modulating the electrolyte thickness, following the protocols indicated in the top panels, for the high-Pt catalyst (a) and the low-Pt catalyst (b). The STEM images were acquired before and after the potential cycling; scale bars, 50 nm. The CV profiles were measured under AST.

destruction of the carbon support (Figure 2a). Under an e-beam dose of 5.47 $e^-/Å^2$ for the same duration, the Pt/C catalyst displayed a slow but noticeable carbon degradation (Figure 2b). However, reducing the e-beam dose further to 2.94 $e^-/Å^2$ resulted in no visible beam-induced structural damage to the Pt/C catalyst even over 5 min (Figure 2c). The lowest e-beam dose resulted in the fewest temporal changes in the catalyst structures, as evidenced by the computed normalized cross-correlation between the initial and subsequent STEM images (Figure 2d). Since capturing a single STEM image in the e-LCTEM took about 30 s, it suggests that the experiments were conducted with minimal e-beam effects. Nonetheless, even limited e-beam irradiation could induce temperature variations in the thin electrolyte, potentially influencing electrochemical reactions. Our methodology mitigates temperature variations, bolstered by two additional key operational protocols. First, electrochemical measurements were performed after replenishing the electrolyte in the liquid-cell, ensuring that any minor temperature fluctuations in the thin electrolyte condition are effectively mitigated by the significantly thicker electrolyte layer.[41] Second, the electrochemical reactions were executed under beam blanking conditions, ensuring no e-beam exposure during CV cycling. Based on these controls, we conducted STEM imaging with an e-beam dose lower than 3 $e^-/Å^2$ in all our e-LCTEM measurements, which ensures that the structural evolution in observing catalysts is mainly attributed to the applied electrochemical polarization.

Degradation Processes of the Pt/C Catalysts. Equipped with our optimized protocols for e-LCTEM studies, we

https://doi.org/10.1021/jacs.4c08825
J. Am. Chem. Soc. XXXX, XXX, XXX−XXX

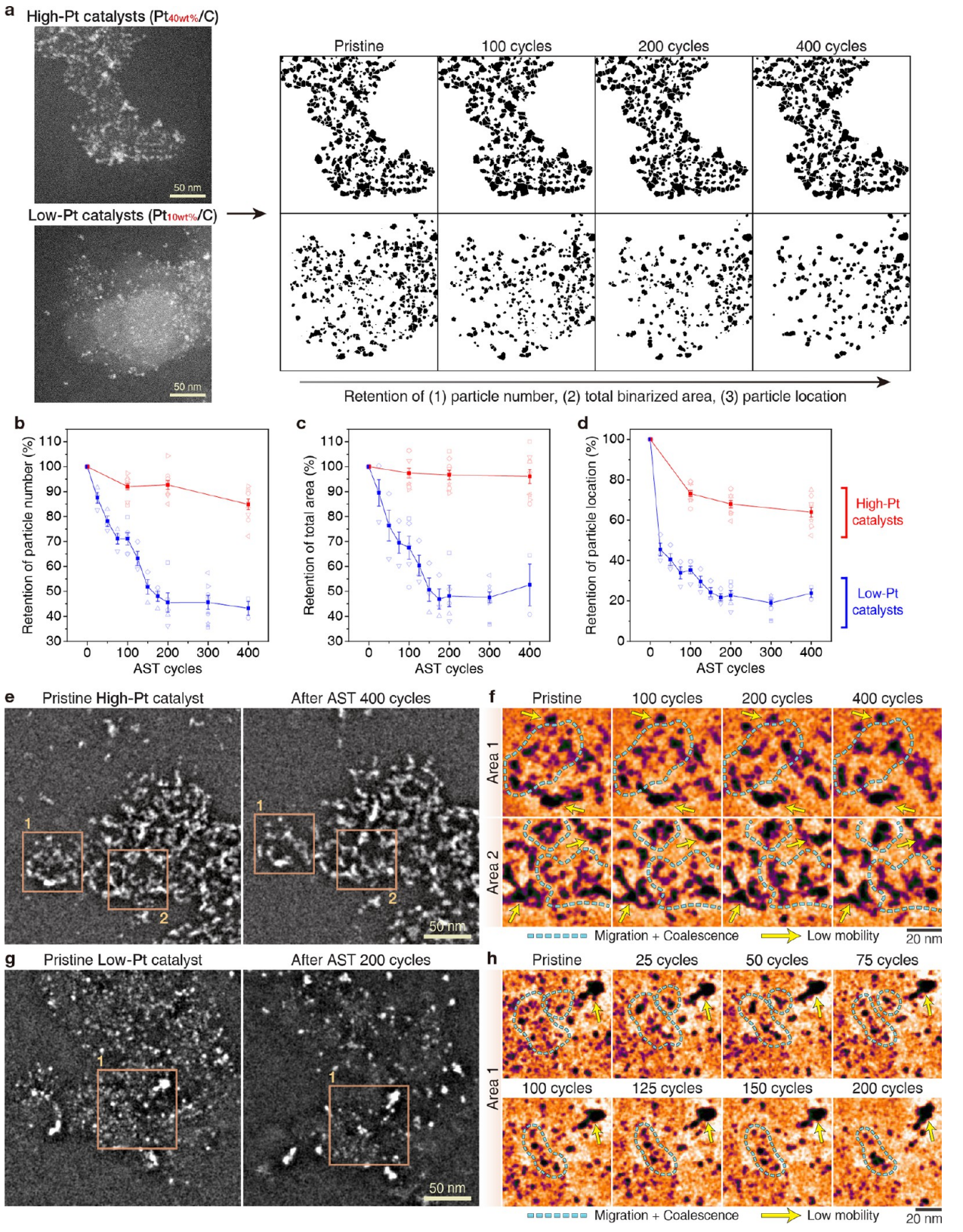

Figure 4. Disparate degradation tendencies of the two commercial catalysts quantified by the binarization of STEM images. (a) Representative examples of binarized STEM images observed in the high-Pt (top row) and the low-Pt catalysts (bottom row); scale bars, 50 nm. (b–d) Changes in retention of the particle number (b), total binarized area (c), and particle locations (d) along AST cycles in several e-LCTEM experiments for the high-Pt (red) and low-Pt (blue) catalysts. Error bars in (b-d) indicate standard errors obtained from multiple replicates. (e,g) Bandpass-filtered and (f,h) LUT-applied STEM cropped images of the high-Pt (e,f) and low-Pt (g,h) catalysts before and after AST. Blue dotted circles represent migration and coalescence of small Pt nanoparticles, and yellow arrows indicate low mobility of larger Pt nanoparticles.

https://doi.org/10.1021/jacs.4c08825
J. Am. Chem. Soc. XXXX, XXX, XXX−XXX

monitored the degradation processes of two benchmarking ORR catalysts, commercial $Pt_{10\ wt\ \%}/C$ (low-Pt) and $Pt_{40\ wt\ \%}/C$ (high-Pt), under a harsh AST condition.[3,5,6,12,20,34,42−48] We iteratively performed STEM imaging and potential cycling between 0.4 and 1.4 V vs RHE, the condition used for simulating start−stop operations of the fuel cell.[19,35,36] This measurement was performed through the optimized electrolyte thinning−refilling procedures, ensuring the acquisition of desirable resolution capable of imaging Pt nanoparticles smaller than 3 nm (top panels in Figure 3a,b) and reliable multiple CV profiles with a marginal shift (Figure 3). Sometimes, a window shift may occur as a result of employing a Pt pseudo-reference electrode, as illustrated in the CV profile labeled as 4 in Figure 3a. However, it remains within the range of ±0.05 V and does not significantly impact the overall degradation trend.

STEM imaging during AST reveals distinct degradation trends for the two model systems. While the high-Pt catalyst exhibited minor displacement of the Pt nanoparticles (Figure 3a), the low-Pt catalyst showed a significant decrease in the number and an enlargement of nanoparticles (Figure 3b and Movie S3). The reduction in the Pt amount aligns with the overlaid CV curve in Figure 3b, displaying a notable decrease in the formation and reduction peaks of Pt oxides (Figure S6). These different degradation trends are further corroborated by independent measurements of ECSA using normal electrochemical setups and additional identical location TEM (IL-TEM) analyses, ensuring the reliability and integrity of our e-LCTEM method. When the same AST condition (0.4−1.4 V vs RHE, 400 cycles) was applied to the model catalysts loaded on a RDE, a higher reduction (60%) of ECSA was recorded in the low-Pt catalyst compared to the other catalyst (33%) (Figure S5 and Materials and Methods, Supporting Information). This large difference in the ECSA is consistent with the distinct degradation trends observed in the e-LCTEM results (Figure S7 and Materials and Methods, Supporting Information). Notably, the pronounced reduction in the ECSA in the low-Pt catalysts aligns with the substantial decrease in the particle number and the particle enlargement observed in e-LCTEM. Additionally, *ex situ* tracking of Pt nanoparticles via IL-TEM revealed a pronounced decrease in the number and enlargement of Pt nanoparticles in the low-Pt catalyst, while the high-Pt catalyst showed minute structural changes (Figure S8 and Materials and Methods, Supporting Information). We recognize that e-beam irradiation on the thin electrolyte can generate small amounts of radiolysis products, potentially affecting the carbon support and particle detachment, even at low e-beam doses. However, the routine introduction of micrometer-thick fresh electrolytes efficiently neutralizes these radiolysis products, ensuring they do not significantly influence the overall degradation trend. This is supported by the consistent findings across both e-LCTEM and IL-TEM studies (Figure S8), which show that our method effectively mitigates the potential impacts of radiolysis on catalyst degradation.

To rigorously assess the degradation pathways of the two catalysts, we conducted a quantitative analysis using binarization techniques on multiple STEM images sourced from various e-LCTEM experiments. In these images, Pt nanoparticles are represented in black (as shown in Figures 4a and S9 and described in Materials and Methods, Supporting Information). For the high-Pt and low-Pt catalysts, image series of 9 and 12 were utilized, respectively (Figures S10−S15). The error bars presented in Figure 4b−d reflect the standard errors calculated for each measurement cycle. The analysis of the binarized images facilitated quantification of catalyst degradation through three principal metrics: the retention of particle numbers, the total binarized area (indicative of the Pt amounts), and the shift in particle location relative to their initial positioning. The retention of particle location was quantitatively assessed by determining the overlap percentage between binarized images of Pt nanoparticles in their pristine state and those after degradation. The number of Pt nanoparticles in the low-Pt catalyst rapidly decreased by ∼50% after AST 400 cycles (Figure 4b), whereas the high-Pt catalyst exhibited a more gradual decline, retaining ∼90% of its particles after the same potential cycling (Figure 4b). Similarly, the total binarized area of the low-Pt catalyst rapidly decreased to ∼50%, indicating a 50% reduction in its amount, while that of the high-Pt catalyst maintained its initial value (Figure 4c). While ∼80% of the Pt nanoparticles in the low-Pt catalyst deviated from their initial positions, only ∼25% of the Pt nanoparticles in the high-Pt were displaced from the original locations (Figure 4d).

The applied AST conditions were capable of simultaneously inducing particle dissolution (Pt dissolution) and particle migration (carbon oxidation). The dissolution-gated degradation mechanism is characterized by the electrochemical dissolution of Pt particles at their surfaces, resulting in the formation of Pt ions. These ions either diffuse into the electrolyte or redeposit onto other particles. This process predominantly occurs at the particle surface rather than near the carbon support, which prevents weakening of the Pt−C interaction and leads to localized Pt dissolution. Conversely, the migration-gated degradation mechanism involves an increased mobility of particles due to the mitigation of the Pt−C interaction caused by carbon oxidation. This increased mobility facilitates the coalescence and detachment of the particles. The fundamental difference between these mechanisms lies in the mobility of the particles driven by changes in the carbon substrate.

To ascertain the dominant degradation mechanism, we evaluated the degradation processes by aligning our experimental data with theoretical models and examining their impact on three specific indicators throughout the AST cycles (Figure S16). Should particle dissolution dominate, we would expect to see a reduction in particle size at fixed locations, significantly diminishing the Pt content while maintaining consistent particle numbers and positions. However, this expected pattern sharply contrasts with our observations (Figure S16). Conversely, if particle migration were the primary degradation mechanism, significant changes in both the particle number and location would be evident, as particularly observed in the low-Pt catalyst. This would likely lead to particle displacement, either toward or away from the carbon support, potentially resulting in enlarged Pt nanoparticles through coalescence and a reduction in their number due to detachment (Figure S16). The more rapid decrease in the retention of particle locations (Figure 4d) compared with the decay in particle numbers (Figure 4b) and total areas (Figure 4c) in the low-Pt catalyst indicates a predominance of migration-induced degradation over dissolution-driven mechanisms. Additionally, trajectories of Pt nanoparticles with sizes ranging from 3 to 4 nm, tracked over cycles of the AST, clearly indicate their migration on the carbon support (Figure S17). Moreover, the observed discrepancies in decay rates among the retention numbers in the high-Pt catalyst further suggest that

https://doi.org/10.1021/jacs.4c08825
J. Am. Chem. Soc. XXXX, XXX, XXX−XXX

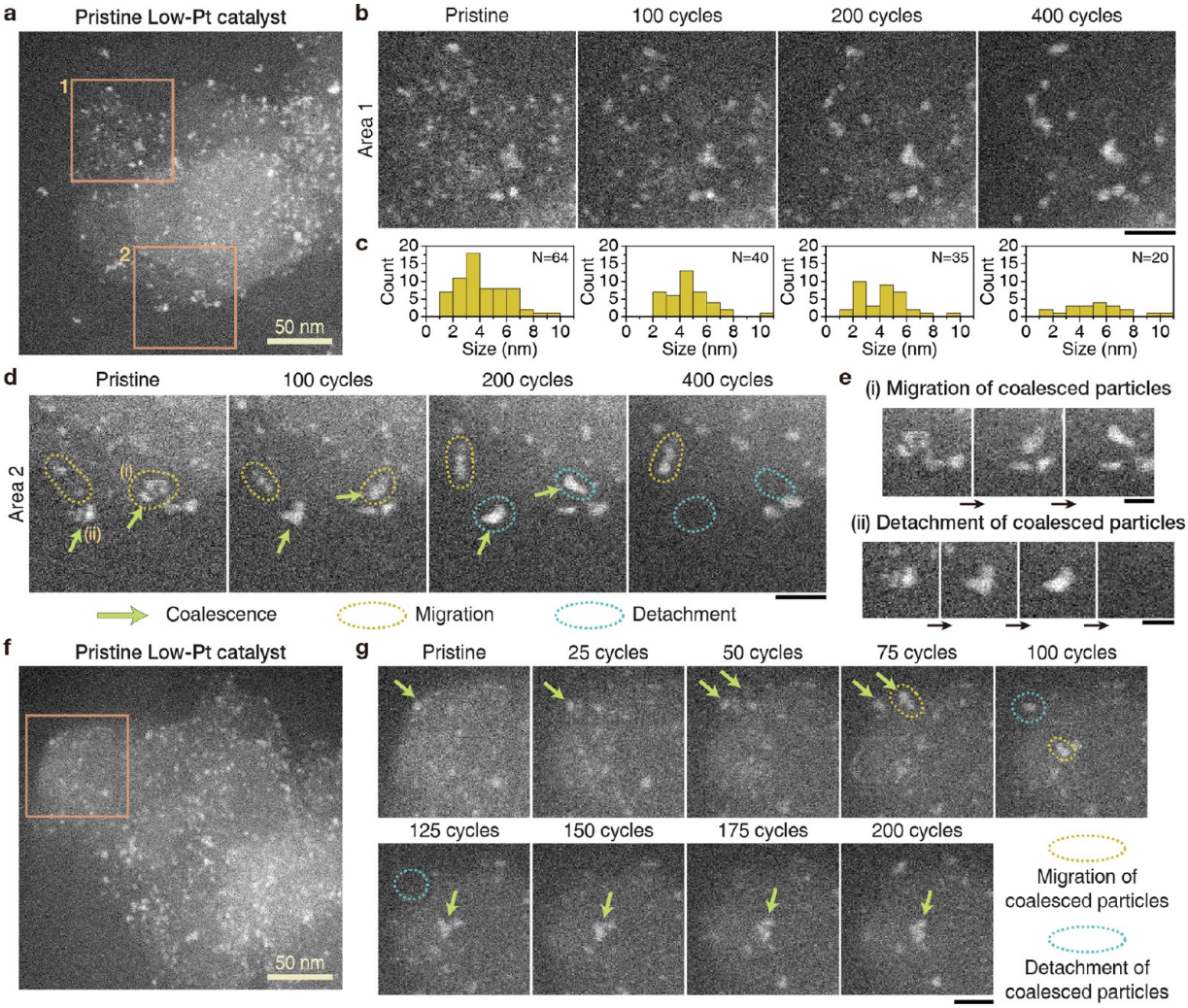

Figure 5. High-resolution STEM tracking of individual nanoparticles in the low-Pt catalysts. (a) A STEM image of low-Pt catalysts at the pristine state; scale bar, 50 nm. (b) Cropped images of area 1 before and after the potential cycling; scale bar, 20 nm. (c) Histograms for the particle size distribution of the cropped STEM images. (d) Cropped images of area 2 before and after the potential cycling; scale bar, 20 nm. Green arrows indicate coalescence of Pt nanoparticles. Yellow and blue dotted circles represent migration and detachment of Pt nanoparticles, respectively. (e) Magnified representations of the sections marked as (i,ii) in the cropped STEM images of area 2 along AST; scale bars, 10 nm. Migration (i) and detachment (ii) of coalesced particles were observed. (f) A STEM image of the low-Pt catalyst at the pristine state; scale bar, 50 nm. (g) Cropped images in the STEM image before and after the potential cycling; scale bar, 20 nm. Yellow and blue dotted circles represent migration and detachment of coalesced particles, respectively.

dissolution-driven mechanisms alone cannot fully explain the degradation observed. While our findings highlight important insights into the role of migration in catalyst degradation, we recognize that our analyses do not definitively rule out the contribution of Pt dissolution to catalyst degradation. Both dissolution and migration likely contribute to catalyst degradation to varying degrees, depending on specific electrochemical operating conditions.

Additionally, we performed additional e-LCTEM experiments with the low-Pt catalyst under mild AST conditions (0.6−0.95 V vs RHE, 500 cycles, see Materials and Methods, Supporting Information).[49] Subsequent STEM imaging revealed smaller displacement and slight enlargement of Pt nanoparticles after this mild AST (Figures S18 and S19). Furthermore, our binarization analysis showed that degradation in both the number and total amount of Pt nanoparticles was approximately two times slower under these mild conditions compared to observations under harsh AST. This data suggests that the lower upper potential limit, which mitigates carbon oxidation, leads to substantially slower catalyst degradation and significantly curtails Pt nanoparticle migration relative to harsh AST conditions. This additional evidence may also support the notion that a dissolution-driven mechanism alone is insufficient to explain the extensive degradation observed in the low-Pt catalyst under harsh AST conditions.

Tracking particles at a fixed localized area revealed their size-dependent mobility, which can explain the different degradation patterns apparent in the two commercial catalysts. We found that small Pt nanoparticles in both low-Pt and high-Pt catalysts commonly exhibit greater mobility than larger Pt nanoparticles within the corresponding samples (Figures 4e−h and S20). Along with different particle size distributions of the low-Pt (2.5 ± 0.6 nm) and the high-Pt catalysts (4.3 ± 0.9 nm) (Figures 3 and S21), the observed averaged higher mobility of the low-Pt then can be attributed to the higher numbers of smaller constituent particles as compared to the high-Pt. Additional e-LCTEM studies of the size-controlled Pt/C

https://doi.org/10.1021/jacs.4c08825
J. Am. Chem. Soc. XXXX, XXX, XXX−XXX

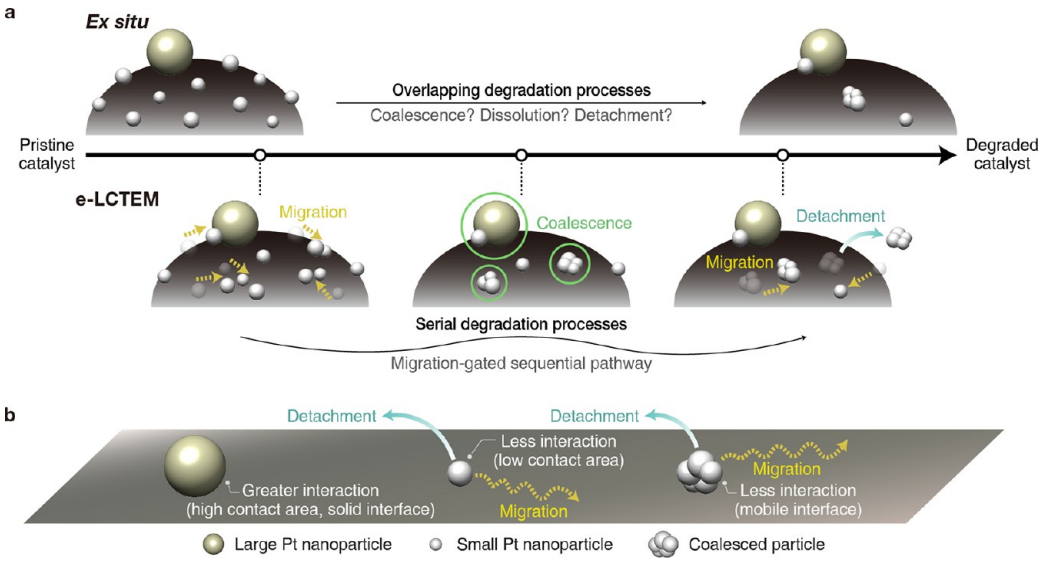

Figure 6. Refined mechanistic picture. (a) A scheme of the difference between *ex situ* TEM (top) and e-LCTEM analysis (bottom) for the catalyst degradation. (b) Refined degradation mechanisms of Pt/C catalysts under the harsh AST.

catalysts (1.9 ± 0.3 vs 5.4 ± 0.8 nm) but with a similar loading amount revealed an identical size-dependent trend, indicating a greater size effect over the effect of loading amount on catalyst degradation (Figure S22a,b).[50,51] While the Pt/C catalyst of smaller nanoparticles exhibited a substantial decrease in the number and an enlargement of Pt nanoparticles after AST 100 cycles (Figure S22c), the Pt/C catalyst of larger nanoparticles underwent minor changes in the number and location of Pt nanoparticles (Figure S22d). This trend is further corroborated by independent measurement of ECSAs using a RDE. After 500 cycles of CV ranging from 0.4 to 1.4 V vs RHE, the Pt/C catalyst of smaller nanoparticles showed a 64% decrease in ECSA, whereas the Pt/C catalyst of larger nanoparticles exhibited only a 23% reduction (Figure S22e,f). The minor impact of the loading amount, in contrast to particle size, is further substantiated by comparing the changes in ECSAs of additional samples prepared to have the same size but different loadings (Figure S23). Taken together, these findings highlight the critical role of the nanoparticulate size in determining the degradation of the Pt/C catalyst, particularly when their migration is a key to the degradation pathways. Additionally, the extent to which each mechanism contributes is influenced by the structural characteristics of Pt nanoparticles and is supported by this size-dependent degradation tendency. Smaller particles in the low-Pt catalysts are more susceptible to carbon oxidation, rendering the migration-gated mechanism predominant and resulting in high particle mobility. In contrast, the high-Pt catalysts, consisting of larger particles, exhibit a reduced contribution to the migration-gated mechanism, leading to low particle mobility.

Direct Monitoring of Serial Degradation Processes. High-resolution STEM tracking of individual Pt nanoparticles (Figure 5) reveals a holistic picture of catalyst degradation and its dynamic nature under polarization. Aligned with the above ensemble analysis conducted on global areas, the focused examination of a local region within the low-Pt catalyst (area 1 in Figure 5a) reveals a reduction in the number of Pt nanoparticles and an increase in their sizes (Figure 5b,c). The changes in the number and size distribution of Pt nanoparticles within the focused areas and its additional IL-TEM (Figure S24) analysis corroborate the prevailing migration-induced degradation, rather than dissolution-driven degradation.[19] Individual particles within the local region (area 2 in Figure 5a) display noticeable migration (yellow dotted lines), which results in subsequent coalescence (green arrows) and detachment (blue dotted lines) (Figure 5d). The coalescence appears to maintain the mobility of the corresponding particles, leading to subsequent migration and their final detachment (Figure 5e). These coupled events in series are generally operative, as evinced by multiple e-LCTEM experiments (Figure 5f,g).

Refined Degradation Pathways. Previous TEM-based analysis offers basic statistics, such as changes in the number and size distribution of nanoparticles, before and after applying electrical bias or electrochemical reactions (Figure 6a, top). The timing of the TEM image acquisition is critical for observing individual elementary degradation pathways before subsequent steps proceed. In many cases of *ex situ* TEM analyses, only an overlap of multiple pathways is captured in each image (Figure 6a, top). For instance, a significant loss in the overall particle number may result not only from dissolution but also from competing particle detachment. Also, the size increment of nanoparticles may stem from particle coalescence or Ostwald ripening. Distinguishing between or quantifying the relative contribution of these individual pathways is critical for unraveling holistic catalyst degradation mechanisms.

Our advanced reliable e-LCTEM methods enable tracking the catalyst degradation under electrochemical polarization at short time intervals with improved resolution. Our analytic protocol facilitates the decoupling of overlapping degradation pathways and the direct observation of sequential processes, thus providing an unprecedented unified picture (Figure 6a, bottom). While Pt dissolution has been suggested as a primary pathway of Pt/C degradation, leading to secondary degradation mechanisms such as Ostwald ripening, there is no indication of prevailing nanoparticulate dissolution in our analysis. Through quantitative and direct imaging analysis at both global areas and single-particle levels, we uncover a distinct catalyst degradation mechanism predominantly gated by the migration of Pt nanoparticles instead. Within this

https://doi.org/10.1021/jacs.4c08825
J. Am. Chem. Soc. XXXX, XXX, XXX−XXX

mechanistic picture, smaller nanoparticles are more susceptible to initial migration than larger particles, and the coalescence of the small nanoparticles enhances mobility, leading to final detachment. While dissolution-driven catalyst degradation has traditionally been explained by the Gibbs−Thomson effect,[45,52] accounting for the size-dependent surface energy of constituent particles, our new proposed mechanism highlights the size-dependent mobility of nanoparticles under the conditions of carbon oxidation or anodic polarization.

The migration-gated degradation likely stems from the carbon oxidation or polarization-induced mitigation of electronic and electrostatic Pt−C interactions under the AST conditions applied in this work (Figure 6b). The magnitude of Pt−C interaction would depend on the strength and extent of attachment of Pt nanoparticles to the carbon support. Smaller nanoparticles, with higher surface energy, may tend to bind more strongly to the support. Conversely, larger nanoparticles, adhering to the carbon supports with a wider contact area, may exhibit greater interaction with the supports. The observed high mobility of small Pt nanoparticles under AST conditions, contrasting with the low mobility of larger particles, implies that particles with numerous adsorption sites on carbon supports are more resistant to catalyst degradation induced by carbon oxidation (Figure 6b, left and middle). Although the high weight of larger Pt nanoparticles may impact their low mobility, considering the high mobility of enlarged particles after coalescence, their influence is presumed to be insignificant. The high mobility of the coalesced particles can be attributed to their weak interaction with the carbon support, likely stemming from structural reorganization during coalescence, accompanied by particle rotation to align lattice mismatches, atomic rearrangement to rectify defective crystal structures, and/or particle reshaping to minimize surface energy.[53−55] This can explain why large particles, after coalescence, exhibit weaker resistance against migration compared to the large particles anchored onto the carbon support in their pristine state (Figure 6b, right). The foregoing discussion strongly suggests that understanding and controlling the polarization-induced dynamics of the interactions between catalysts and support materials should be very critical for attaining optimal durability of supported catalysts under polarization.

CONCLUSIONS

We report a novel e-LCTEM technique integrated with advanced sample preparation and *in situ* thickness control of the electrolyte, which enables a time-series analysis of high-resolution STEM images for small nanoparticles (<3 nm) while ensuring reliable electrochemical reactions. Using this advanced tool, we explore the degradation processes of representative ORR catalysts, comprising Pt nanoparticles with varying sizes and Pt loading amounts on carbon supports, under AST conditions that simulate start−stop operations of the fuel cell. Our analytic protocol applied for this system facilitates decoupling of overlapped degradation pathways and direct observation of sequential processes, thus providing an unprecedented holistic mechanistic picture. Through quantitative and direct imaging analysis at both global areas and single-particle levels, we uncover a distinct catalyst degradation pathway predominantly gated by migration of Pt nanoparticles. We observe that smaller nanoparticles display greater susceptibility to migration, resulting in their successive coalescence and detachment. This migration-driven degradation mechanism, likely originating from polarization-induced mitigation of Pt−C interactions, provides a novel perspective on the size-dependent durability of supported nanocatalysts, complementing prevailing explanations based on the size-dependent dissolution kinetics. Ultimately, this study suggests that controlling the polarization-induced dynamics of the interaction between catalysts and support materials could offer a way to achieve optimal durability of supported catalysts under electrochemical polarization conditions.

ASSOCIATED CONTENT

Supporting Information

The Supporting Information is available free of charge at https://pubs.acs.org/doi/10.1021/jacs.4c08825.

Experimental details, materials, and methods; photographs of e-LCTEM microchips and an aligner; CV profiles measured in e-LCTEM and bulk experiments; e-LCTEM images; IL-TEM images; representations for all steps of STEM image binarization; structure analysis for the two commercial Pt/C catalysts; and additional experiments with size-controlled Pt/C catalysts (PDF)

Movie for the a slow generation of a bubble within the liquid-cell[2] (MP4)

STEM movie for the Pt/C catalysts under e-beam irradiation with different e-beam doses (MP4)

STEM movie for the degradation of Low-Pt catalysts under the harsh AST condition (MP4)

AUTHOR INFORMATION

Corresponding Authors

Young-Jung Heo − *Advanced Fuel Cell Technology Development Team 1, R&D division, Hyundai Motor Company, Yongin 16891, Republic of Korea;* orcid.org/0000-0003-2851-3484; Email: youngjungheo@hyundai.com

Jaeyune Ryu − *Department of Chemical and Biological Engineering, Institute of Chemical Processes, Seoul National University, Seoul 08826, Republic of Korea; Center for Nanocrystal Research, Institute for Basic Science (IBS), Seoul 08826, Republic of Korea*; Email: jaeyune.ryu@snu.ac.kr

Jungwon Park − *Department of Chemical and Biological Engineering, Institute of Chemical Processes, Seoul National University, Seoul 08826, Republic of Korea; Center for Nanocrystal Research, Institute for Basic Science (IBS), Seoul 08826, Republic of Korea; Institute of Engineering Research, College of Engineering, Seoul National University, Seoul 08826, Republic of Korea; Advanced Institute of Convergence Technology, Seoul National University, Suwon 16229, Republic of Korea;* orcid.org/0000-0003-2927-4331; Email: jungwonpark@snu.ac.kr

Authors

Sungin Kim − *Department of Chemical and Biological Engineering, Institute of Chemical Processes, Seoul National University, Seoul 08826, Republic of Korea; Center for Nanocrystal Research, Institute for Basic Science (IBS), Seoul 08826, Republic of Korea; Department of Chemistry and Chemical Biology, Cornell University, Ithaca, New York 14853, United States;* orcid.org/0000-0001-9107-0781

Jimin Kwag − *Department of Chemical and Biological Engineering, Institute of Chemical Processes, Seoul National University, Seoul 08826, Republic of Korea; Center for*

https://doi.org/10.1021/jacs.4c08825
J. Am. Chem. Soc. XXXX, XXX, XXX−XXX

Nanocrystal Research, Institute for Basic Science (IBS), Seoul 08826, Republic of Korea; Department of Chemical Engineering, Massachusetts Institute of Technology, Cambridge, Massachusetts 02139, United States

Minyoung Lee − *Department of Chemical and Biological Engineering, Institute of Chemical Processes, Seoul National University, Seoul 08826, Republic of Korea; Center for Nanocrystal Research, Institute for Basic Science (IBS), Seoul 08826, Republic of Korea*

Sungsu Kang − *Department of Chemical and Biological Engineering, Institute of Chemical Processes, Seoul National University, Seoul 08826, Republic of Korea; Center for Nanocrystal Research, Institute for Basic Science (IBS), Seoul 08826, Republic of Korea; Department of Chemistry, University of Chicago, Chicago, Illinois 60637, United States*

Dongjun Kim − *Department of Chemical and Biological Engineering, Institute of Chemical Processes, Seoul National University, Seoul 08826, Republic of Korea; Center for Nanocrystal Research, Institute for Basic Science (IBS), Seoul 08826, Republic of Korea*

Jong-Gil Oh − *Advanced Fuel Cell Technology Development Team 1, R&D division, Hyundai Motor Company, Yongin 16891, Republic of Korea*

Complete contact information is available at: https://pubs.acs.org/10.1021/jacs.4c08825

Notes

The authors declare no competing financial interest.

■ ACKNOWLEDGMENTS

This work was supported by the Institute for Basic Science (IBS-R006-D1) and the National Research Foundation of Korea (NRF) grant funded by the Korean Government (MSIT) (Grant No. NRF-2021M3H4A1A02049904 and RS-2024-00421181). Additionally, this work was also supported by the Hyundai Motor Company. J.R. acknowledges the Creative-Pioneering Researchers Program (0458-20240094) through Seoul National University (SNU).

■ REFERENCES

(1) Martín, A. J.; Mitchell, S.; Mondelli, C.; Jaydev, S.; Pérez-Ramírez, J. Unifying views on catalyst deactivation. *Nat. Catal.* **2022**, *5* (10), 854−866.

(2) Kodama, K.; Nagai, T.; Kuwaki, A.; Jinnouchi, R.; Morimoto, Y. Challenges in applying highly active Pt-based nanostructured catalysts for oxygen reduction reactions to fuel cell vehicles. *Nat. Nanotechnol.* **2021**, *16* (2), 140−147.

(3) Zhang, J. W.; Yuan, Y. L.; Gao, L.; Zeng, G. M.; Li, M. F.; Huang, H. W. Stabilizing Pt-Based Electrocatalysts for Oxygen Reduction Reaction: Fundamental Understanding and Design Strategies. *Adv. Mater.* **2021**, *33* (20), 2006494.

(4) Zhao, Z.; Liu, Z.; Zhang, A.; Yan, X.; Xue, W.; Peng, B.; Xin, H. L.; Pan, X.; Duan, X.; Huang, Y. Graphene-nanopocket-encaged PtCo nanocatalysts for highly durable fuel cell operation under demanding ultralow-Pt-loading conditions. *Nat. Nanotechnol.* **2022**, *17*, 968−975.

(5) Chen, F. D.; Chen, S. G.; Wang, A. X.; Wang, M.; Guo, L.; Wei, Z. D. Blocking the sulfonate group in Nafion to unlock platinum's activity in membrane electrode assemblies. *Nat. Catal.* **2023**, *6* (5), 392−401.

(6) Huang, J.; Sementa, L.; Liu, Z. Y.; Barcaro, G.; Feng, M.; Liu, E. S.; Jiao, L.; Xu, M. J.; Leshchev, D.; Lee, S. J.; Li, M. F.; Wan, C. Z.; Zhu, E. B.; Liu, Y.; Peng, B. S.; Duan, X. F.; Goddard, W. A.; Fortunelli, A.; Jia, Q. Y.; Huang, Y. Experimental Sabatier plot for predictive design of active and stable Pt-alloy oxygen reduction reaction catalysts. *Nat. Catal.* **2022**, *5*, 513−523.

(7) Li, Y. Z.; Li, Y. B.; Cui, Y. Catalyst: How Cryo-EM Shapes the Development of Next-Generation Batteries. *Chem* **2018**, *4* (10), 2250−2252.

(8) Lazouski, N.; Chung, M. J.; Williams, K.; Gala, M. L.; Manthiram, K. Non-aqueous gas diffusion electrodes for rapid ammonia synthesis from nitrogen and water-splitting-derived hydrogen. *Nat. Catal.* **2020**, *3* (5), 463−469.

(9) Chang, W. S.; Jain, A.; Rezaie, F.; Manthiram, K. Lithium-mediated nitrogen reduction to ammonia via the catalytic solid-electrolyte interphase. *Nat. Catal.* **2024**, *7*, 231−241.

(10) Cargnello, M.; Doan-Nguyen, V. V. T.; Gordon, T. R.; Diaz, R. E.; Stach, E. A.; Gorte, R. J.; Fornasiero, P.; Murray, C. B. Control of Metal Nanocrystal Size Reveals Metal-Support Interface Role for Ceria Catalysts. *Science* **2013**, *341* (6147), 771−773.

(11) Sytwu, K.; Vadai, M.; Dionne, J. A. Bimetallic nanostructures: combining plasmonic and catalytic metals for photocatalysis. *Adv. Phys.:X* **2019**, *4* (1), 1619480.

(12) Zhu, E. B.; Wu, M. H.; Xu, H. Z.; Peng, B. S.; Liu, Z. Y.; Huang, Y.; Li, Y. J. Stability of Platinum-Group-Metal-based Electrocatalysts in Proton Exchange Membrane Fuel Cells. *Adv. Funct. Mater.* **2022**, *32* (30), 2203883.

(13) Jayabal, S.; Saranya, G.; Geng, D. S.; Lin, L. Y.; Meng, X. B. Insight into the correlation of Pt-support interactions with electrocatalytic activity and durability in fuel cells. *J. Mater. Chem. A* **2020**, *8* (19), 9420−9446.

(14) Wang, X. Q.; Li, Z. J.; Qu, Y. T.; Yuan, T. W.; Wang, W. Y.; Wu, Y.; Li, Y. D. Review of Metal Catalysts for Oxygen Reduction Reaction: From Nanoscale Engineering to Atomic Design. *Chem* **2019**, *5* (6), 1486−1511.

(15) Arán-Ais, R. M.; Yu, Y. C.; Hovden, R.; Solla-Gullón, J.; Herrero, E.; Feliu, J. M.; Abruña, H. D. Identical Location Transmission Electron Microscopy Imaging of Site-Selective Pt Nanocatalysts: Electrochemical Activation and Surface Disordering. *J. Am. Chem. Soc.* **2015**, *137* (47), 14992−14998.

(16) Goodman, E. D.; Johnston-Peck, A. C.; Dietze, E. M.; Wrasman, C. J.; Hoffman, A. S.; Abild-Pedersen, F.; Bare, S. R.; Plessow, P. N.; Cargnello, M. Catalyst deactivation via decomposition into single atoms and the role of metal loading. *Nat. Catal.* **2019**, *2* (9), 748−755.

(17) Castanheira, L.; Dubau, L.; Mermoux, M.; Berthomé, G.; Caqué, N.; Rossinot, E.; Chatenet, M.; Maillard, F. Carbon Corrosion in Proton-Exchange Membrane Fuel Cells: From Model Experiments to Real-Life Operation in Membrane Electrode Assemblies. *ACS Catal.* **2014**, *4* (7), 2258−2267.

(18) Labata, M. F.; Li, G. F.; Ocon, J.; Chuang, P. Y. A. Insights on platinum-carbon catalyst degradation mechanism for oxygen reduction reaction in acidic and alkaline media. *J. Power Sources* **2021**, *487*, 229356.

(19) Meier, J. C.; Galeano, C.; Katsounaros, I.; Topalov, A. A.; Kostka, A.; Schüth, F.; Mayrhofer, K. J. J. Degradation Mechanisms of Pt/C Fuel Cell Catalysts under Simulated Start-Stop Conditions. *ACS Catal.* **2012**, *2* (5), 832−843.

(20) Yang, Y.; Xiong, Y.; Zeng, R.; Lu, X.; Krumov, M.; Huang, X.; Xu, W.; Wang, H.; DiSalvo, F. J.; Brock, J. D.; Muller, D. A.; Abruña, H. D. Operando Methods in Electrocatalysis. *ACS Catal.* **2021**, *11*, 1136−1178.

(21) Shen, T. H.; Spillane, L.; Peng, J. Y.; Shao-Horn, Y.; Tileli, V. Switchable wetting of oxygen-evolving oxide catalysts. *Nat. Catal.* **2022**, *5* (1), 30−36.

(22) Park, H.; Jeon, Y.; Chung, W. J.; Bae, Y.; Kim, J.; Baek, H.; Park, J. Early Stage Li Plating by Liquid Phase and Cryogenic Transmission Electron Microscopy. *ACS Energy Lett.* **2023**, *8* (1), 715−721.

(23) Yang, Y.; Louisia, S.; Yu, S.; Jin, J.; Roh, I.; Chen, C.; Fonseca Guzman, M. V.; Feijoo, J.; Chen, P. C.; Wang, H.; Pollock, C. J.; Huang, X.; Shao, Y. T.; Wang, C.; Muller, D. A.; Abruna, H. D.; Yang,

P. Operando studies reveal active Cu nanograins for CO_2 electroreduction. *Nature* **2023**, *614*, 262−269.
(24) Yang, Y.; Shao, Y. T.; Lu, X. Y.; Yang, Y.; Ko, H. Y.; DiStasio, R. A.; DiSalvo, F. J.; Muller, D. A.; Abruña, H. D. Elucidating Cathodic Corrosion Mechanisms with Operando Electrochemical Transmission Electron Microscopy. *J. Am. Chem. Soc.* **2022**, *144* (34), 15698−15708.
(25) Yang, F.; Lopez Luna, M.; Haase, F. T.; Escalera-López, D.; Yoon, A.; Rüscher, M.; Rettenmaier, C.; Jeon, H. S.; Ortega, E.; Timoshenko, J.; Bergmann, A.; Chee, S. W.; Roldan Cuenya, B. Spatially and Chemically Resolved Visualization of Fe Incorporation into NiO Octahedra during the Oxygen Evolution Reaction. *J. Am. Chem. Soc.* **2023**, *145* (39), 21465−21474.
(26) de Jonge, N.; Ross, F. M. Electron microscopy of specimens in liquid. *Nat. Nanotechnol.* **2011**, *6*, 695−704.
(27) Lee, S. Y.; Shangguan, J. Y.; Betzler, S.; Harris, S. J.; Doeff, M. M.; Zheng, H. M. Lithium metal stripping mechanisms revealed through electrochemical liquid cell electron microscopy. *Nano Energy* **2022**, *102*, 107641.
(28) Kato, H. In-Situ Liquid TEM Study on the Degradation Mechanism of Fuel Cell Catalysts. *SAE Int. J. Alt. Power.* **2016**, *5*, 189−194.
(29) Beermann, V.; Holtz, M. E.; Padgett, E.; de Araujo, J. F.; Muller, D. A.; Strasser, P. Real-time imaging of activation and degradation of carbon supported octahedral Pt-Ni alloy fuel cell catalysts at the nanoscale using in situ electrochemical liquid cell STEM. *Energy Environ. Sci.* **2019**, *12* (8), 2476−2485.
(30) Impagnatiello, A.; Cerqueira, C. F.; Coulon, P. E.; Morin, A.; Escribano, S.; Guetaz, L.; Clochard, M. C.; Rizza, G. Degradation Mechanisms of Supported Pt Nanocatalysts in Proton Exchange Membrane Fuel Cells: An Operando Study through Liquid Cell Transmission Electron Microscopy. *ACS Appl. Energy Mater.* **2020**, *3* (3), 2360−2371.
(31) Nagashima, S.; Ikai, T.; Sasaki, Y.; Kawasaki, T.; Hatanaka, T.; Kato, H.; Kishita, K. Atomic-Level Observation of Electrochemical Platinum Dissolution and Redeposition. *Nano Lett.* **2019**, *19* (10), 7000−7005.
(32) Hodnik, N.; Dehm, G.; Mayrhofer, K. J. J. Importance and Challenges of Electrochemical *in Situ* Liquid Cell Electron Microscopy for Energy Conversion Research. *Acc. Chem. Res.* **2016**, *49* (9), 2015−2022.
(33) Zhu, G. Z.; Prabhudev, S.; Yang, J.; Gabardo, C. M.; Botton, G. A.; Soleymani, L. In Situ Liquid Cell TEM Study of Morphological Evolution and Degradation of Pt-Fe Nanocatalysts During Potential Cycling. *J. Phys. Chem. C* **2014**, *118* (38), 22111−22119.
(34) Soleymani, A. P.; Parent, L. R.; Jankovic, J. Challenges and Opportunities in Understanding Proton Exchange Membrane Fuel Cell Materials Degradation Using In-Situ Electrochemical Liquid Cell Transmission Electron Microscopy. *Adv. Funct. Mater.* **2022**, *32* (5), 2105188.
(35) Zana, A.; Speder, J.; Roefzaad, M.; Altmann, L.; Bäumer, M.; Arenz, M. Probing Degradation by IL-TEM: The Influence of Stress Test Conditions on the Degradation Mechanism. *J. Electrochem. Soc.* **2013**, *160* (6), F608−F615.
(36) Mayrhofer, K. J. J.; Meier, J. C.; Ashton, S. J.; Wiberg, G. K. H.; Kraus, F.; Hanzlik, M.; Arenz, M. Fuel cell catalyst degradation on the nanoscale. *Electrochem. Commun.* **2008**, *10* (8), 1144−1147.
(37) Garsany, Y.; Baturina, O. A.; Swider-Lyons, K. E.; Kocha, S. S. Experimental Methods for Quantifying the Activity of Platinum Electrocatalysts for the Oxygen Reduction Reaction. *Anal. Chem.* **2010**, *82* (15), 6321−6328.
(38) Bhuvanendran, N.; Ravichandran, S.; Xu, Q.; Maiyalagan, T.; Su, H. E. A quick guide to the assessment of key electrochemical performance indicators for the oxygen reduction reaction: A comprehensive review. *Int. J. Hydrogen Energy* **2022**, *47* (11), 7113−7138.
(39) de Jonge, N.; Houben, L.; Dunin-Borkowski, R. E.; Ross, F. M. Resolution and aberration correction in liquid cell transmission electron microscopy. *Nat. Rev. Mater.* **2019**, *4* (1), 61−78.
(40) Ambrožič, B.; Prašnikar, A.; Hodnik, N.; Kostevšek, N.; Likozar, B.; Rožman, K. Ž.; Šturm, S. Controlling the radical-induced redox chemistry inside a liquid-cell TEM. *Chem. Sci.* **2019**, *10*, 8735−8743.
(41) Attri, P.; Kim, Y. H.; Park, D. H.; Park, J. H.; Hong, Y. J.; Uhm, H. S.; Kim, K.-N.; Fridman, A.; Choi, E. H. Generation mechanism of hydroxyl radical species and its lifetime prediction during the plasma-initiated ultraviolet (UV) photolysis. *Sci. Rep.* **2015**, *5*, 9332.
(42) Hartl, K.; Hanzlik, M.; Arenz, M. IL-TEM investigations on the degradation mechanism of Pt/C electrocatalysts with different carbon supports. *Energy Environ. Sci.* **2011**, *4* (1), 234−238.
(43) Huang, L.; Zaman, S.; Tian, X. L.; Wang, Z. T.; Fang, W. S.; Xia, B. Y. Advanced Platinum-Based Oxygen Reduction Electrocatalysts for Fuel Cells. *Acc. Chem. Res.* **2021**, *54* (2), 311−322.
(44) Meier, J. C.; Galeano, C.; Katsounaros, I.; Witte, J.; Bongard, H. J.; Topalov, A. A.; Baldizzone, C.; Mezzavilla, S.; Schüth, F.; Mayrhofer, K. J. J. Design criteria for stable Pt/C fuel cell catalysts. *Beilstein J. Nanotechnol.* **2014**, *5*, 44−67.
(45) Holby, E. F.; Sheng, W. C.; Shao-Horn, Y.; Morgan, D. Pt nanoparticle stability in PEM fuel cells: influence of particle size distribution and crossover hydrogen. *Energy Environ. Sci.* **2009**, *2* (8), 865−871.
(46) Yu, K.; Groom, D. J.; Wang, X. P.; Yang, Z. W.; Gummalla, M.; Ball, S. C.; Myers, D. J.; Ferreira, P. J. Degradation Mechanisms of Platinum Nanoparticle Catalysts in Proton Exchange Membrane Fuel Cells: The Role of Particle Size. *Chem. Mater.* **2014**, *26* (19), 5540−5548.
(47) Du, L.; Prabhakaran, V.; Xie, X.; Park, S.; Wang, Y.; Shao, Y. Low-PGM and PGM-Free Catalysts for Proton Exchange Membrane Fuel Cells: Stability Challenges and Material Solutions. *Adv. Mater.* **2021**, *33* (6), 1908232.
(48) Ott, S.; Orfanidi, A.; Schmies, H.; Anke, B.; Nong, H. N.; Hübner, J.; Gernert, U.; Gliech, M.; Lerch, M.; Strasser, P. Ionomer distribution control in porous carbon-supported catalyst layers for high-power and low Pt-loaded proton exchange membrane fuel cells. *Nat. Mater.* **2020**, *19*, 77−85.
(49) Wang, X.; Hu, L.; Neyerlin, K. C.; Ahluwalia, R. K. Baselining Activity and Stability of ORR Catalysts and Electrodes for Proton Exchange Membrane Fuel Cells for Heavy-Duty Applications. *J. Electrochem. Soc.* **2023**, *170*, 024503.
(50) Inaba, M.; Zana, A.; Quinson, J.; Bizzotto, F.; Dosche, C.; Dworzak, A.; Oezaslan, M.; Simonsen, S. B.; Kuhn, L. T.; Arenz, M. The Oxygen Reduction Reaction on Pt: Why Particle Size and Interparticle Distance Matter. *ACS Catal.* **2021**, *11* (12), 7144−7153.
(51) Quinson, J.; Kunz, S.; Arenz, M. Surfactant-Free Colloidal Syntheses of Precious Metal Nanoparticles for Improved Catalysts. *ACS Catal.* **2023**, *13* (7), 4903−4937.
(52) Shao-Horn, Y.; Sheng, W. C.; Chen, S.; Ferreira, P. J.; Holby, E. F.; Morgan, D. Instability of Supported Platinum Nanoparticles in Low-Temperature Fuel Cells. *Top. Catal.* **2007**, *46*, 285−305.
(53) Song, M.; Zhou, G.; Lu, N.; Lee, J.; Nakouzi, E.; Wang, H.; Li, D. Oriented attachment induces fivefold twins by forming and decomposing high-energy grain boundaries. *Science* **2020**, *367*, 40−45.
(54) Dachraoui, W.; Henninen, T. R.; Keller, D.; Erni, R. Multi-step atomic mechanism of platinum nanocrystals nucleation and growth revealed by in-situ liquid cell STEM. *Sci. Rep.* **2021**, *11*, 23965.
(55) Li, D.; Nielsen, M. H.; Lee, J. R. I.; Frandsen, C.; Banfield, J. F.; De Yoreo, J. J. Direction-Specific Interactions Control Crystal Growth by Oriented Attachment. *Science* **2012**, *336*, 1014−1018.

https://doi.org/10.1021/jacs.4c08825
J. Am. Chem. Soc. XXXX, XXX, XXX−XXX